

Article

Lanthanum-Containing Magnesium Alloy with Antitumor Function Based on Increased Reactive Oxygen Species

Cijun Shuai ^{1,2,3}, Long Liu ², Youwen Yang ¹, Chengde Gao ², Mingchun Zhao ⁴, Lu Yi ^{1,*} and Shuping Peng ^{5,*}

¹ Jiangxi University of Science and Technology, Ganzhou 341000, China; shuai@csu.edu.cn (C.S.); yangyouwen@csu.edu.cn (Y.Y.)

² State Key Laboratory of High Performance Complex Manufacturing, College of Mechanical and Electrical Engineering, Central South University, Changsha 410083, China; liulong@csu.edu.cn (L.L.); gaochengde@csu.edu.cn (C.G.)

³ Shenzhen Institute of Information Technology, Shenzhen 518172, China

⁴ School of Material Science and Engineering, Central South University, Changsha 410083, China; mczhao@csu.edu.cn

⁵ School of Basic Medicine, Central South University, Changsha 410013, China

* Correspondence: 9120030064@jxust.edu.cn (L.Y.); shuping@csu.edu.cn (S.P.); Tel.: +86-731-8480-5412 (L.Y.); Fax: +86-731-8887-9044 (L.Y.)

Received: 27 September 2018; Accepted: 25 October 2018; Published: 1 November 2018



Abstract: Developing antitumor implants is of great significance to repair tumor-induced bone defects and simultaneously prevent bone tumor recurrence. The tumor cells, compared to normal cells, have a high reactive oxygen species level. They are vulnerable to oxidative insults under increased intrinsic oxidative stress. The lanthanum (La) ion with high phospholipid binding ability can open the mitochondrial permeability transition pore, which blocks the electron transport chain in the mitochondria, and consequently increases reactive oxygen species level. In this study, La was alloyed to Mg-6Zn-0.5Zr (ZK60) through selective laser melting technology. The results indicated that the mitochondrial membrane potential dropped whilst the reactive oxygen species increased as the La content increased. ZK60-1.0La revealed a high cell inhibition rate of 61.9% for bone tumor cell and high cell viability of 91.9% for normal cells, indicating that the alloy could induce bone tumor cell death, as well as exhibit good biocompatibility for normal cell. In addition, its degradation rate 1.23 mm/year was lower than that of ZK60 alloy 2.13 mm/year, which was mainly attributed to the grain refinement.

Keywords: antitumor implants; lanthanum; reactive oxygen species; biocompatibility; degradation resistance

1. Introduction

Currently, surgical resection is a popular treatment method for tumor-induced bone defects [1,2]. Nevertheless, the surgical resection cannot eliminate bone tumor cells completely. The residual bone tumor cells may lead to the relapse of the bone tumor [3,4]. Therefore, it is important to develop antitumor implants to repair bone defects and prevent bone tumor relapse [5,6]. Ma et al. have reported that a bifunctional graphene oxide-modified β -tricalcium phosphate implant showed excellent photothermal effects in killing bone-tumor cells, which could be used for therapy of tumor-related bone defects [2]. Li et al. also reported that zoledronic acid-loaded magnesium–strontium alloys could inhibit giant bone cell tumors, which could be a potential implant in repairing the bone defects after

tumor removal [7]. Compared to normal cells, hydrogen peroxide levels are greatly increased in many types of cancer cells [8]. It helps cancer cells to infiltrate and metastasize to other tissues, and hydrogen peroxide is also an important signal molecule regulating the entire process of tumor cell survival, proliferation, and apoptosis [9,10]. As tumor cells have elevated reactive oxygen species levels and are under increased intrinsic oxidative stress, this provides an opportunity to kill the tumor cells based on their vulnerability to reactive oxygen species insults [11–13].

Lanthanum (La), a rare earth element, has received increasing attention due to its antitumor property [14,15]. The radius and valence of the La ion are 1.061 Å and trivalent, respectively [16–18]. The La ion possesses a large ratio of the electric charge to ion radius, enabling a high ability to bind to the divalent metal binding sites on mitochondria. This binding leads to irreversible alteration of its structure and loss of biological activity, which results in disruption of tumor cell function and death [19,20]. Heffeter et al. reported that lanthanum compounds could selectively inhibit or kill tumor cells even in drug-resistant tumor cells [21]. Chen et al. reported that lanthanum chloride could inhibit proliferation and induce the cervical tumor cells death [22]. Considering the antitumor property of La, it is reasonable to speculate that La could be used as an antitumor agent to grant implants the ability to kill bone tumor cells.

As promising bone implant materials, magnesium (Mg) and its alloys possess degradability, good biocompatibility, and desirable mechanical properties [23–26]. They can gradually degrade in the human body, thereby avoiding the second surgery for implant removal and decreasing the pain for patients [27,28]. Mg as a necessary element in the human body can promote new bone formation, which is beneficial to bone defects repairing [29,30]. Furthermore, Mg alloys possess similar elastic modulus and density to those of natural human bones, thus mitigating the stress shielding effect induced by serious mismatch in modulus between implants and natural bones [31]. To our knowledge, there are very few reports about the antitumor property of Mg alloy containing La [32,33].

In this study, La was alloyed to Mg-6Zn-0.5Zr (wt %, ZK60) through a selective laser melting technique to endow it with antitumor properties. Meanwhile, alloying is an effective approach to enhance the Mg degradation resistance by tailoring the phase morphology, distribution, potential, and size of the matrix [34,35]. The antitumor property of ZK60-La was evaluated and the potential mechanisms were discussed. Furthermore, the degradation properties were investigated.

2. Experimental Methods

2.1. Preparation of ZK60-La Samples

The spherical Mg-6Zn-0.5Zr (ZK60) powder (mean particle size 50 µm) (Figure 1a) (Tangshan Weihao Materials Co., Ltd., Tangshan, China) and polyangular La powder (mean particle size 8 µm) (Figure 1b) (Shanghai Naiou Nano technology Co., Ltd., Shanghai, China) were used as raw materials. These two powders were blended homogeneously using ball milling at a rate of 100 rpm for 10 h under argon gas protection to obtain mixed powders with different La contents (0.5, 1.0, 1.5 and 2.0 wt %).

The selective laser melting system (Figure 1c) was composed of a fiber laser, an optical focus system, an automatic powder dispensing apparatus, an argon gas protection device, and a computer-based control setup system [36]. Selective laser melting was carried out in the following parameters: Laser beam diameter 100 µm, laser power 70 W, scanning speed 600 mm/min, and scan line spacing 50 µm. The building chamber was filled with argon gas to prevent oxidation. Then, ZK60 and ZK60-*x*La (*x* = 0.5, 1.0, 1.5 and 2.0 wt %) samples (10 × 10 × 5 mm³) were prepared. The surface of as-built samples was completely dense with no obvious pores or cracks (Figure 1d).

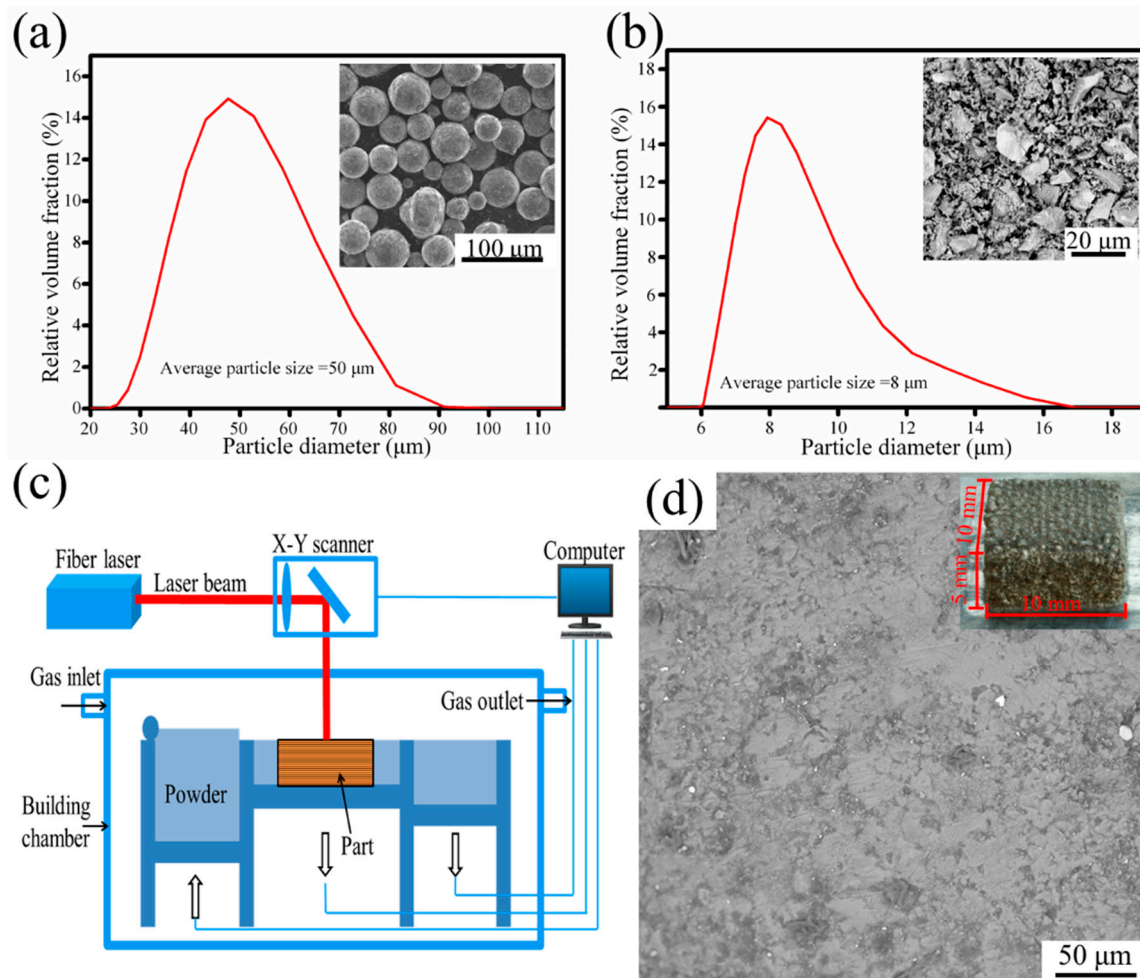


Figure 1. Particle size distributions of powders: (a) ZK60 and (b) La; (c) schematic of selective laser melting system; (d) the surface of the selective laser melted sample.

2.2. Microstructure Characterization and Mechanical Properties Tests

The samples were polished on abrasive papers and finally etched with the picral solution for 10 s. Subsequently their metallurgical structure was observed by optical microscopy. The composition distribution was studied using a scanning electron microscopy (SEM, QUANTA FEG250, FEI Company, Hillsboro, OR, USA) equipped with an energy dispersive spectroscopy (EDS, JSM-5910LV, JEOL, Tokyo, Japan) detector. The phase compositions were analyzed through X-ray diffraction (XRD; Rigaku D/Max 2550, Tokyo, Japan). The hardness was carried out using a HXD-1000TM/LCD device (Shanghai Taiming Optical Instrument Co., Ltd, Shanghai, China) (load of 2.942 N). The compressive strength test was operated at a constant crosshead speed (0.2 mm/min) using an Instron machine (AG-5000G, Shimadzu, Japan).

2.3. Degradation Properties Assays

The potentiodynamic polarization curves were performed using an electrochemical workstation (Gamry 2000+, Gamry, Warminster, PA, USA) with a standard three-electrode configuration. To obtain a stable open circuit potential, the samples were immersed in the simulated body fluid (SBF) solution for 5 min. Then, the measurement was conducted in a potential ranging from -300 mV to 300 mV compared to the open circuit potential. The potentiodynamic scanning rate for the test was 1 mV/s. The corrosion current density (i_{corr}) and corrosion potential (E_{corr}) were obtained through Tafel extrapolation method.

Immersion tests were carried out in SBF solution at 37 ± 0.5 °C. The ratio of the exposed area to the volume of SBF solution was $1.25 \text{ cm}^2/\text{mL}$. Each specimen was immersed in SBF solution for 14 days, then removed from the solution and subsequently washed with distilled water 3 times. The morphology and the composition of the degradation product film on sample surface were assessed by SEM and EDS. After immersion for 3 days, 7 days, and 14 days, each specimen was removed from the solution. The degradation products were removed by immersing the samples in chromic acid solution for 20 min for the weight loss test. The weight loss rate ΔW ($\text{mg}/\text{cm}^2/\text{day}$) was calculated by the formula given in Reference [37]. The degradation rate (P_w , mm/year) was calculated based on the weight loss rate by the equation: $P_w = 2.10\Delta W$, as in Reference [38].

2.4. Antitumor Property and Cytocompatibility

2.4.1. Preparation of ZK60-La Extracts

The extracts for the antitumor tests were conducted as follows. ZK60 and ZK60-La samples were sterilized using ultraviolet radiation for 1 h. Then the samples were immersed in Dulbecco's modified Eagle's medium (DMEM) for 5 days, and the extraction medium ratio (the specimen surface area/medium volume) was kept at $1.25 \text{ cm}^2/\text{mL}$. All the extracts were subsequently centrifuged at 3000 rpm for 5 min, collecting supernates, and adding 10% fetal bovine serum (FBS). The pH values of the extracts were characterized by a pH meter. The ion concentrations of the extracts were analyzed by an inductively coupled plasma-atomic emission spectroscopy.

2.4.2. Cell Culture

The human osteosarcoma cells (U2OS cells) were purchased from the Type Culture Collection of the Chinese Academy of Sciences. Cells were maintained in DMEM supplemented with 10% FBS in a humidified atmosphere with 5% CO_2 at 37 °C. The medium was changed every two or three days. Human embryonic kidney 293 cells (HEK 293 cells) were purchased from Chinese Infrastructure of Cell Line Resources. The cells were cultured at 37 °C in a humidified atmosphere of 5% CO_2 . The cell culture medium used was DMEM supplemented with 10% FBS.

2.4.3. CCK8 Assay

The U2OS cells were adopted to evaluate the antitumor property. DMEM with 10% fetal bovine serum was used as blank control. U2OS cells (2×10^4 cells/mL) were seeded in 96-well plates and cultured with DMEM supplemented with 10% FBS for 24 h. The incubated medium was then substituted by 200 μL of ZK60 or ZK60-La extracts. At 1 day, 3 days, and 5 days, the incubated medium was then removed and 200 μL medium containing 10 μL cell counting kit-8 (CCK-8) solution (Dojindo Laboratories, Tokyo, Japan) was introduced, followed by continuous incubation for another 2 h. Optical density (OD) values at 570 nm were obtained through a microplate reader. The relative growth rate (RGR) of cells was calculated according to the equation: $\text{RGR} = (\text{OD of the sample}/\text{OD of blank control group}) \times 100\%$. Human embryonic kidney 293 cells (HEK 293 cells) were used to assess the cytocompatibility. The cells (1×10^5 cells/mL) were incubated in a 96-well plate for 24 h. Then, 100 μL of extracts were added to each well to replace the medium. Then, 10 μL CCK-8 solution was added to each well after incubating for 1 day, 3 days, and 5 days, and subsequently incubated for another 2 h. OD values at 570 nm were obtained using a microplate reader.

2.4.4. Live/Dead Cell Staining

For live/dead staining studies, tumor cells (1×10^5 cells/mL) were seeded in 24-well plates cultured in an incubator for 24 h to allow attachment, and then, 200 μL extracts were added to each well to replace the medium. Subsequently, the medium was removed and the live/dead staining was performed with 0.2 ml of combination dye (Live/Dead Cell Viability Assay, Invitrogen). Briefly, 1 μM calcein AM and 2 μM ethidium homodimer-1 solutions were prepared in PBS. After the removal of the

extracts medium, the cells were washed with PBS solution for three times, followed by addition of 100 μL of 1 μM calcein AM and 2 μM ethidium homodimer-1 solution. The fluorescent images of cells were then taken by a fluorescence microscope (BX60, Olympus, Japan). The viable cells combined with calcein-AM were stained green, whereas the dead cells combined with ethidium homodimer-1 were stained red. For live/dead staining studies, HEK 293 cells (1×10^5 cells/mL) were seeded in 24-well plates for 24 h, and then, 200 μL extracts were added to each well to replace the medium. Subsequently, the medium was removed and the live/dead staining was performed.

2.4.5. Detection of Changes in Mitochondrial Membrane Potential

The potential of mitochondrial membrane was detected by the mitochondrial permeability JC-1 fluorescent dye. Briefly, cells (5×10^3 cells/mL) were seeded into a 96-well plate in 200 μL medium for 24 h. Then, 400 μL of extracts were added to each well to replace the medium and the cells were cultured for further 24 h. Then, the medium was then replaced by 10 μL of 5 mmol/L JC-1 staining solution, and the plate was incubated for 15 min at 37 ± 0.5 °C. The plate was centrifuged for 5 min and the supernatant was removed, and then, 200 μL of PBS solution was added. Cells were resuspended in 1 mL PBS, and instantly assessed with flow cytometry.

2.4.6. Measurement of Reactive Oxygen Species

The reactive oxygen species (ROS) level was detected using a 6-carboxy-2',7'-dichlorodihydrofluorescein diacetate (DCFH-DA) fluorescent probe. Cells were cultured in 6-well plates and allowed to attach. Cells were washed with PBS solution after culturing with extract for 24 h. Subsequently, they were incubated with DCFH-DA solution (10 $\mu\text{mol/L}$ in DMEM) for 20 min at 37 ± 0.5 °C. Afterward, cells were washed twice with PBS solution to remove the excess staining solution and instantly assessed with flow cytometry. Differential expression was expressed as the ratio of the fluorescence intensity of experimental samples to the fluorescence intensity of the control sample.

2.5. Statistical Analysis

Data were expressed as mean \pm standard deviation of three independent experiments. The statistical differences were analyzed between different groups to determine the p values by Student's t test, which were considered significant when a p value < 0.05 .

3. Results and Discussion

3.1. Antitumor Property

The fluorescence images of the U2OS cells after culturing in the different extracts for 5 days are shown in Figure 2a–f. No dead cells were observed in the control group (Figure 2a). Few dead cells were observed in the ZK60 extract (Figure 2b). Significantly, dead cells gradually increased and live cells decreased in ZK60-La extracts with La content increasing. In addition, the cells cultured in the ZK60-La extracts exhibited an unhealthy shrinkage shape. These results indicated that ZK60-La exhibited antitumor property, and higher La content exhibited higher antitumor efficiency.

The cell viabilities of the U2OS cells were studied by CCK8 assay, with results shown in Figure 2g. The cell viability of the U2OS cells after culturing in ZK60 extract for 5 days was 94.2%. As a comparison, the cell viability of the U2OS cells cultured in ZK60-0.5La, ZK60-1.0La, ZK60-1.5La, and ZK60-2.0La extracts were 50.8%, 38.1%, 31.4%, and 25.2%, respectively. It indicated that the alloying of La inhibited the growth of U2OS cells, and the cell inhibition rate gradually increased with La content increasing. Among these, ZK60-1.0La extract exhibited a cell inhibition rate of 61.9%. These results were in accordance with the fluorescence staining test.

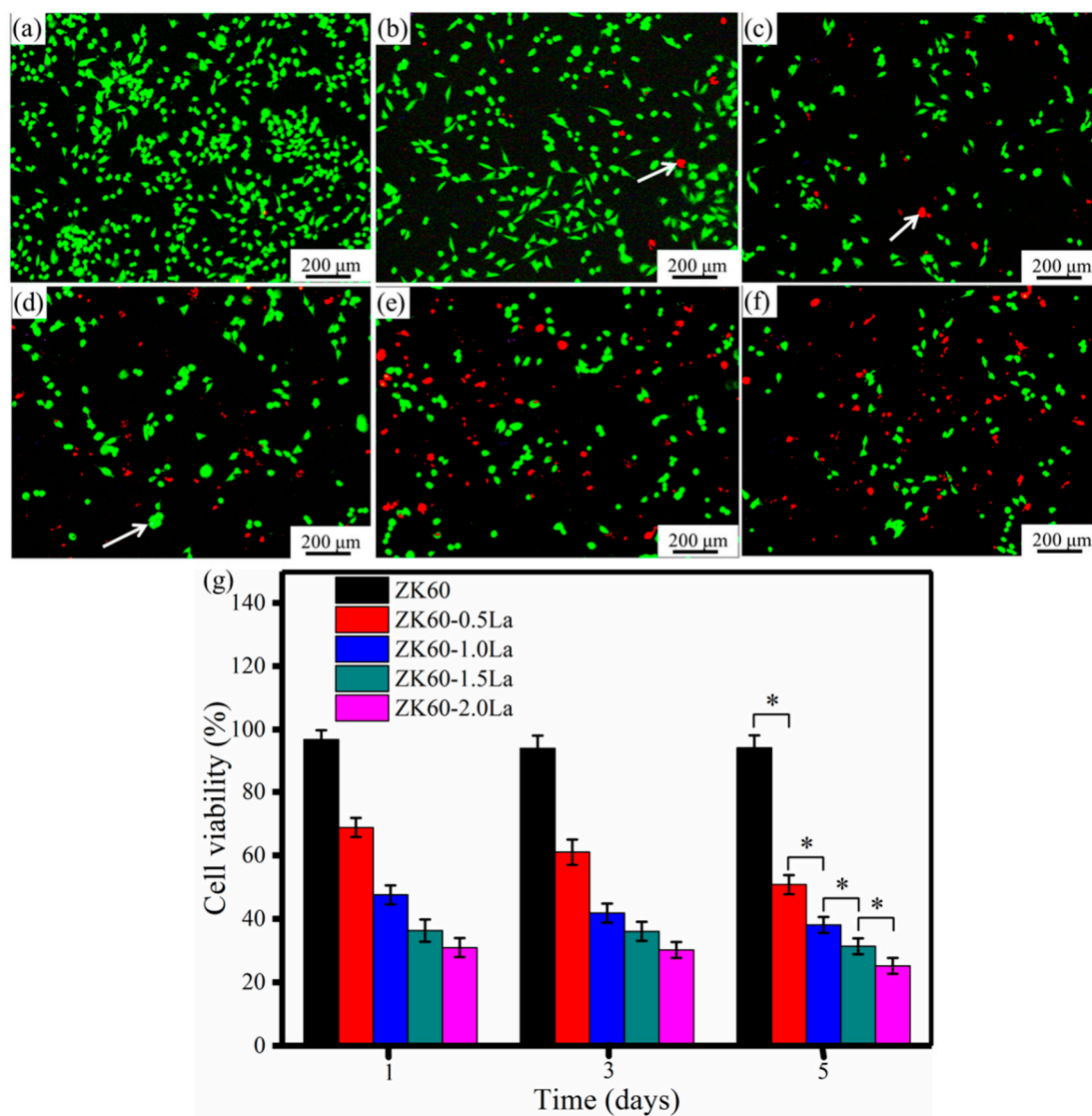


Figure 2. U2OS cells after culturing in extracts for 5 days and stained with live/dead assay; red represented the dead cells and green represented the live cells: (a) Control (b) ZK60, (c) ZK60-0.5La, (d) ZK60-1.0La, (e) ZK60-1.5La, (f) ZK60-2.0La; (g) cell viability of U2OS cells in different extracts after culturing for 1 day, 3 days, and 5 days.

The fluorescence images of the HEK 293 cells after culturing in the different extracts for 5 days were exhibited in Figure 3a–f. From the results of live/dead staining, almost no dead cells were observed. The morphology of the cells was in spindle-like shape after culturing in different extracts, which indicated that the ZK60-La exhibited compatibility to normal cells. The CCK8 assay was used to assess the cytocompatibility for HEK 293 cells, with results shown in Figure 3g. The cell viability of HEK 293 cells after culturing in extract of ZK60, ZK60-0.5La, ZK60-1.0La, ZK60-1.5La, and ZK60-2.0La for 5 days was 80.3%, 88.9%, 91.9%, 90.3%, and 84.4%, respectively. The viabilities of the cells cultured in ZK60-La extract were higher than 80% (grade 1, according to the Standard [39]), indicating that ZK60-La showed no toxicity to HEK 293 cells.

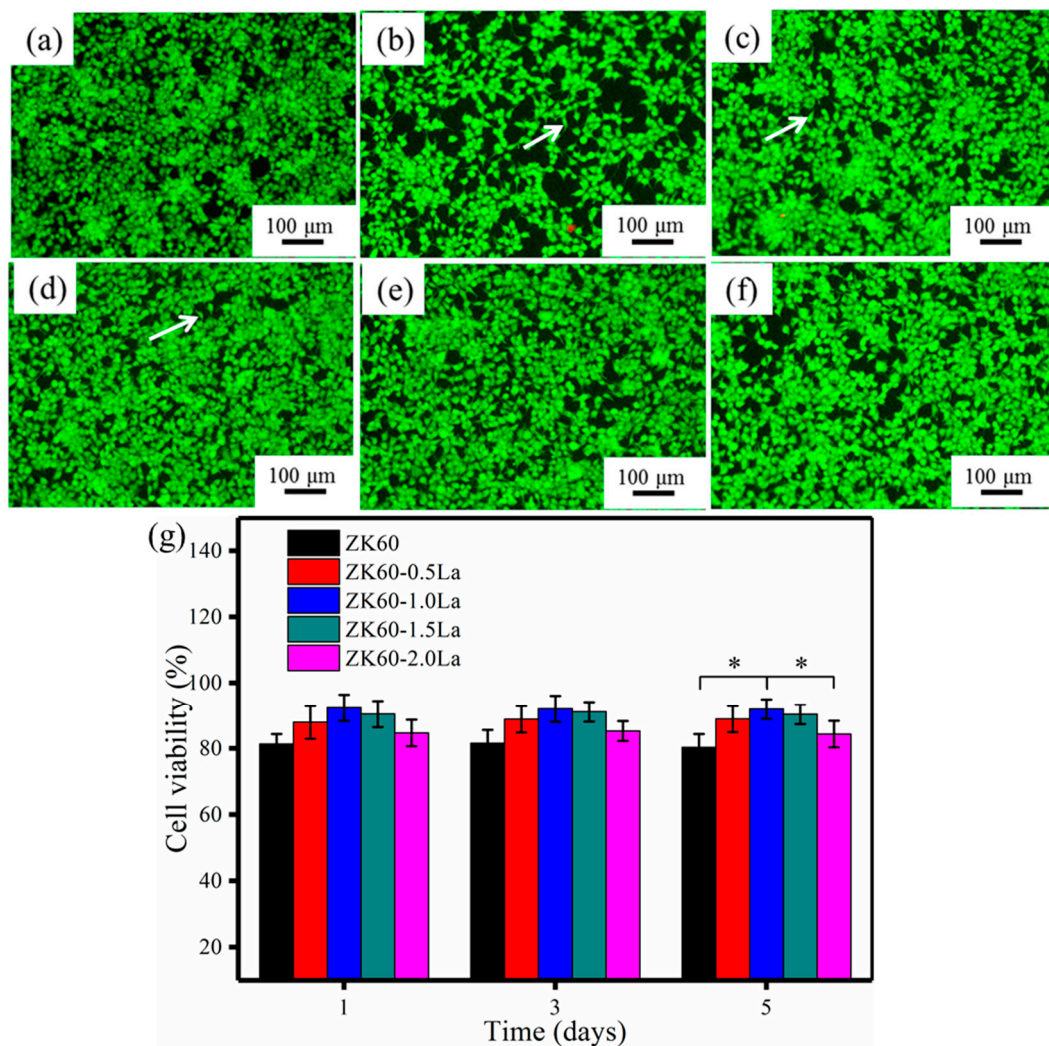


Figure 3. HEK 293 cells after culturing in extracts for 5 days and stained with live/dead assay; red represented the dead cells and green represented the live cells: (a) Control (b) ZK60, (c) ZK60-0.5La, (d) ZK60-1.0La, (e) ZK60-1.5La, (f) ZK60-2.0La; (g) cell viability of HEK 293 cells in different extracts after culturing for 1 day, 3 days and 5 days.

Compared to normal cells, tumor cells had a high ROS level, and were more vulnerable to oxidative insults under increased intrinsic oxidative stress. It was well known that the mitochondria were the main ROS factory in the cells. Thus, the level of mitochondrial membrane potential (MMP) and that of ROS in U2OS cells were measured. As shown in Figure 4a, the level of MMP after incubating in ZK60 extract was 95.2%, and the level of MMP decreased in the U2OS cells with the La content increasing. Specifically, the obtained MMP in the extract of ZK60-La was reduced to 88.6% for ZK60-0.5La, 80.2% for ZK60-1.0La, 76.7% for ZK60-1.5La, and 73.2% for ZK60-2.0La, respectively. Meanwhile, the ROS levels in U2OS cells after incubating in the different extracts are shown in Figure 4b. The ROS level after incubating in ZK60 extract was 109.2%, and the ROS level increased in the U2OS cells with the La content increasing. Specifically, the obtained ROS level in the extract of ZK60-La was increased to 122.3% for ZK60-0.5La, 138.5% for ZK60-1.0La, 145.8% for ZK60-1.5La, and 152.1% for ZK60-2.0La, respectively.

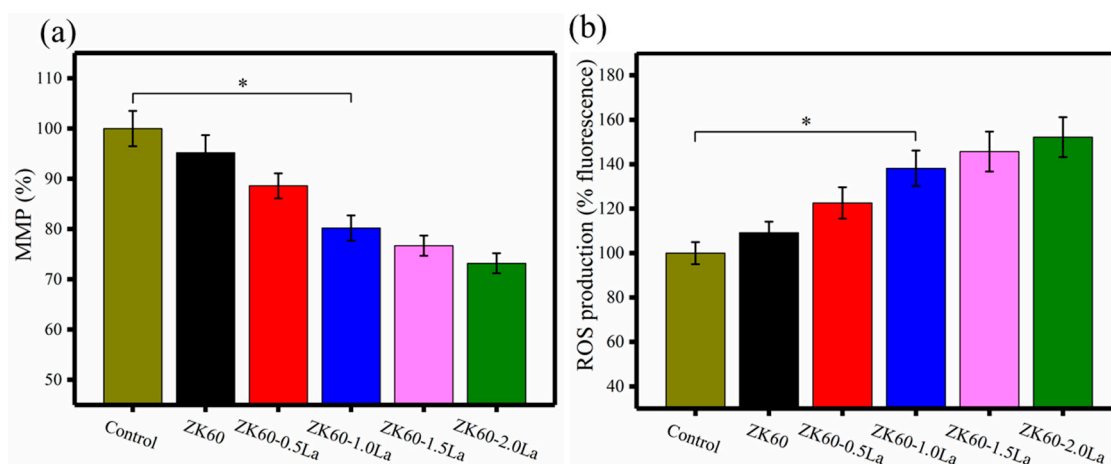


Figure 4. (a) The mitochondrial membrane potential (MMP) and (b) reactive oxygen species (ROS) in U2OS cells after incubating in the different extracts.

The degradation of Mg metals led to metal ions release accompanied by high alkalinity, which might be key factors causing cell death. The pH value of the ZK60 and ZK60-La extracts after immersing for 5 days is shown in Figure 5A. The pH value of the ZK60 extract was 8.8. The pH values of ZK60-La extracts were lower than that of the ZK60 extract, and pH value of ZK60-1.0La extract was 8.2, which was the lowest among them. It could be inferred that ZK60-1.0La had the slowest degradation rate and the least OH^- release, providing a more favorable environment for cell growth. Thus, HEK 293 cells exhibited the highest cell viability in ZK60-1.0La extract. The ion concentrations of the extracts were illustrated in Figure 5B. The La ion concentrations in ZK60-La extracts were $0.5 \pm 0.1 \mu\text{g}/\text{mL}$ for ZK60-0.5La alloy, $1.2 \pm 0.2 \mu\text{g}/\text{mL}$ for ZK60-1.0La alloy, $1.9 \pm 0.1 \mu\text{g}/\text{mL}$ for ZK60-1.5La alloy, and $3.5 \pm 0.1 \mu\text{g}/\text{mL}$ for ZK60-2.0La alloy. The concentration of La ion increased with the La content increasing in ZK60-La. Although higher concentrations of La ions were more conducive to killing tumor cells, they also impaired the biocompatibility of ZK60-La [40].

The mechanism of ZK60-La inducing tumor cell death is illustrated in Figure 5C. The ZK60-La released a mass of La^{3+} when they degraded. The La^{3+} was transported into the tumor cell through the ion channels on the cell membrane. The radius of the La^{3+} (1.061 \AA) were close to that of calcium ion (Ca^{2+}) (0.99 \AA) [41]. However, the La^{3+} possessed the greater ratio of the electric charge to radius ($3/1.061 \text{ \AA} = 2.83$) than that of the Ca^{2+} ($2/0.99 \text{ \AA} = 2.02$), which made it possess a stronger bonding force with divalent binding sites than the Ca^{2+} [42]. Thus, the La^{3+} could replace the Ca^{2+} binding to the binding sites on the mitochondrial permeability transition pore (mPTP) [43]. The opening of mPTP could result in ionic balance disorders between the mitochondrial matrix and cytoplasm. The redistribution of ions on both sides of the membrane led to the decrease of mitochondrial membrane potential. As a result, the electron transport chain was blocked, which resulted in the reactive oxygen species generation. In addition, the ability to scavenge free radicals for cells could also be weakened in a high alkaline environment by suppressed activity of related enzymes in cells, leading to the reactive oxygen species accumulation [44]. The ROS accumulated in the tumor cells could result in oxidative stress, regulating the expression of related proteins, finally causing tumor cell apoptosis. The apoptosis was a typically form of programmed cell death regulated by genes, which played a role in the cell death. A local burst of ROS also could induce oxidation of nucleotides in DNA [45]. Irreparable DNA damage prevented proper protein synthesis, which led to cell death [46].

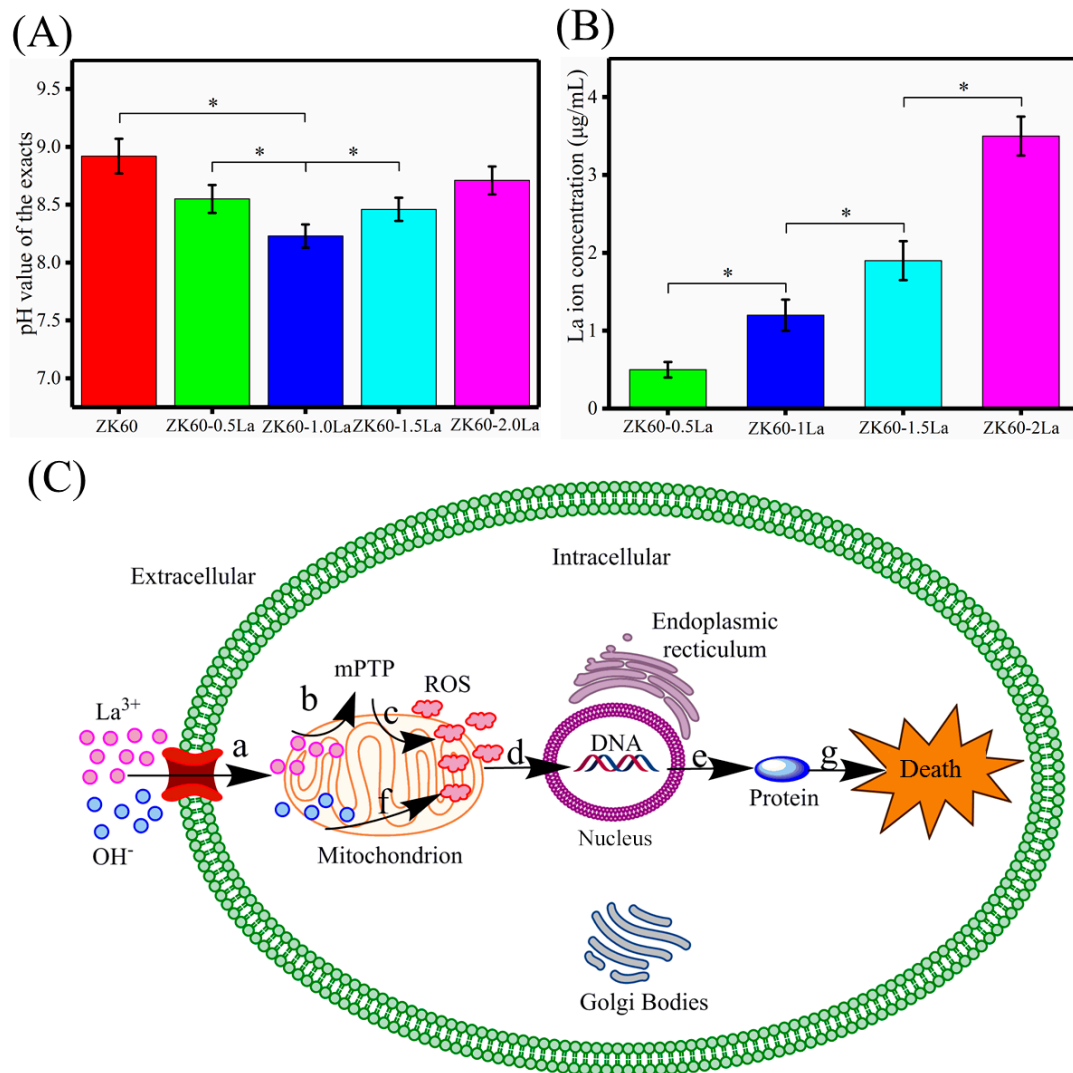


Figure 5. Characterization of the extracts: (A) pH value; (B) La^{3+} concentration; (C) Mechanism of ZK60-La inducing tumor cell death: (a) La^{3+} and OH^- transported into cell; (b) the mitochondrial permeability transition pore (mPTP) opening; (c) ROS accumulated in mitochondrion; (d) regulated the gene expression; (e) regulated the expression levels of protein; (f) ROS accumulation caused by OH^- ; and (g) regulation of protein expression led cell death.

3.2. Degradation Properties

The polarization curves of ZK60 and ZK60-La immersed in SBF are presented in Figure 6a. The E_{corr} and I_{corr} estimated using Tafel extrapolation are shown in Table 1. The E_{corr} and I_{corr} of ZK60 were -1.61 V and $50.2 \mu\text{A}/\text{cm}^2$. It should be noted that ZK60-1.0La had the highest E_{corr} (-1.41 V) and the lowest I_{corr} ($26.3 \mu\text{A}/\text{cm}^2$), which suggested that it had the best degradation resistance.

The degradation rate of ZK60 and ZK60-La calculated from the weight loss are exhibited in Figure 6b. The degradation rate increased with the immersion time increasing from 3 to 7 days, while it decreased with the increasing immersion time from 7 to 14 days. It could be attributed to the reduction of surface area for the samples in the degradation process. When the samples immersed in the solution, the surface of the sample was exposed to the solution causing several thermodynamic reactions, thus increasing the degradation rate. While, protective films would form on the samples after prolonged immersion in SBF, which prohibited the contact between the samples and corrosive medium, thus decreasing the degradation rate. The degradation rate of ZK60 was $2.13 \text{ mm}/\text{year}$ after exposure to SBF for 14 days. When the content of La increased to 1.0 wt %, the degradation rate decreased to

1.23 mm/year. Clearly, various La content exerted an effect on the pH of extract, as shown in Figure 5A. With La content increasing to 1.0 wt %, the degradation rate was reduced. Thus, the released OH^- was decreased. With La content further increased, the degradation was accelerated, and the pH value was consequently increased.

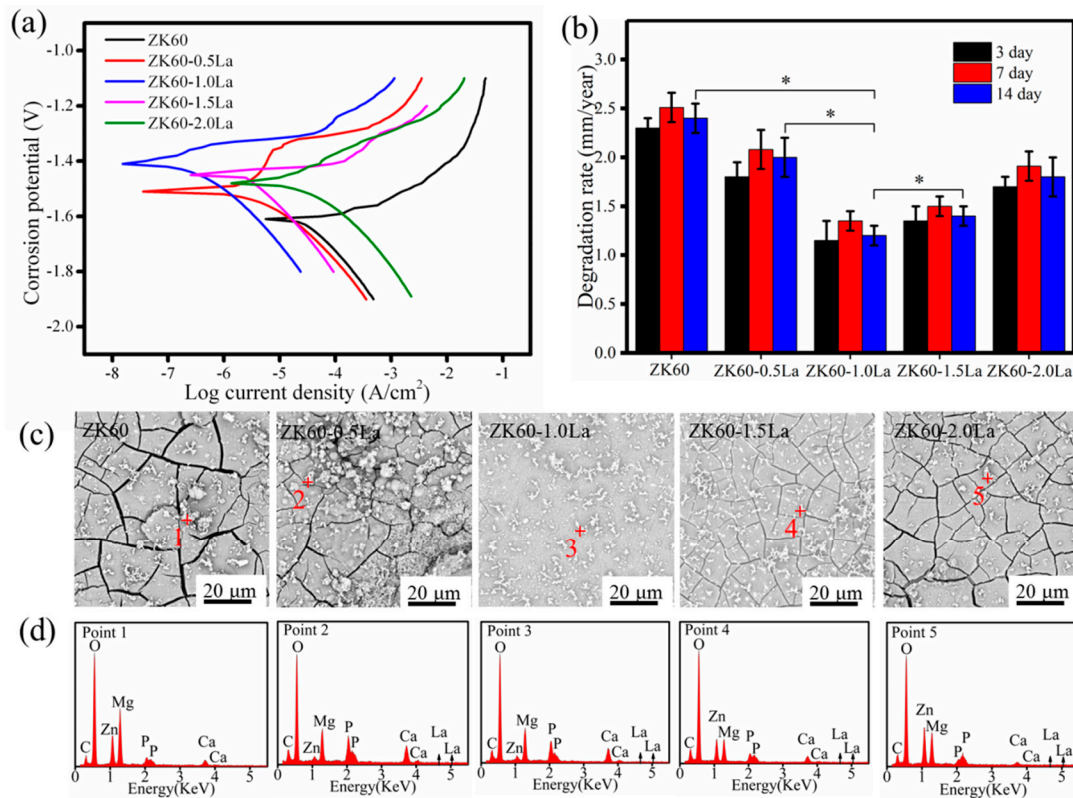


Figure 6. (a) Polarization curves of ZK60 and ZK60-La immersed in SBF solution; (b) Degradation rates of ZK60 and ZK60-La calculated from the weight loss; (c) Morphology of the ZK60 and ZK60-La after immersing in SBF solution for 14 days; (d) Energy dispersive spectroscopy (EDS) spectra of the degradation products indicated by the red point in Figure 6c.

Table 1. The corrosion potential and current density of ZK60 and ZK60-La estimated using Tafel extrapolation.

	E_{corr} (V)	I_{corr} ($\mu\text{A}/\text{cm}^2$)
ZK60	-1.61 ± 0.01	50.2 ± 7
ZK60-0.5La	-1.51 ± 0.01	39.4 ± 5
ZK60-1.0La	-1.41 ± 0.01	26.3 ± 3
ZK60-1.5La	-1.45 ± 0.01	35.1 ± 5
ZK60-2.0La	-1.48 ± 0.01	43.7 ± 5

The morphology of ZK60 and ZK60-La after immersing in SBF solution for 14 days is shown in Figure 6c. They were all covered with degradation product layer. Many cracks were observed for ZK60, while the surface film of ZK60-1.0La maintained integrity. The EDS spectra of the degradation products are shown in Figure 6c. Corresponding EDS data were listed in Table 2. It is shown that the degradation products were primarily constituted of O, C, and Mg. The La and Zn, along with Ca, P, were also detected in the degradation products. The atomic ratio of Ca to P was about 1.34, which is between the Ca/P ratios of octacalcium phosphate and hydroxyapatite.

Table 2. EDS results of the degradation products indicated by the red point in Figure 6c.

Point	Mg	Zn	La	C	O	Ca	P
	at%	at%	at%	at%	at%	at%	at%
1	14.72	4.62	-	17.90	58.37	2.51	1.88
2	7.15	0.89	0.30	18.72	61.34	6.61	4.99
3	8.07	1.12	0.45	17.32	62.69	5.79	4.56
4	6.50	3.79	0.21	21.42	21.42	2.90	2.25
5	10.05	6.25	0.84	21.49	58.20	1.61	1.56

3.3. Microstructure

The metallurgical structure of ZK60 and ZK60-La obtained by optical microscopy are shown in Figure 7. Both ZK60 and ZK60-La consisted of dendrite grains and intermetallics. The average grain size was 13.1 μm for ZK60, 10.2 μm for ZK60-0.5La, 7.6 μm for ZK60-1.0La, 6.3 μm for ZK60-1.5La, and 5.1 μm for ZK60-2.0La, respectively. The results showed that alloying La to the ZK60 contributed to grain refinement. The related refinement mechanism was as follows: During solidification, the solute La atoms possessed strong segregation ability and formed constitutional undercooling in a diffusion layer. The constitutional undercooling could reduce the diffusion rate of solute atoms, which restricted grain growth and promoted the primary Mg matrix nucleation. Moreover, the La-containing intermetallic could form at grain boundary, which could further prevent the grain growth.

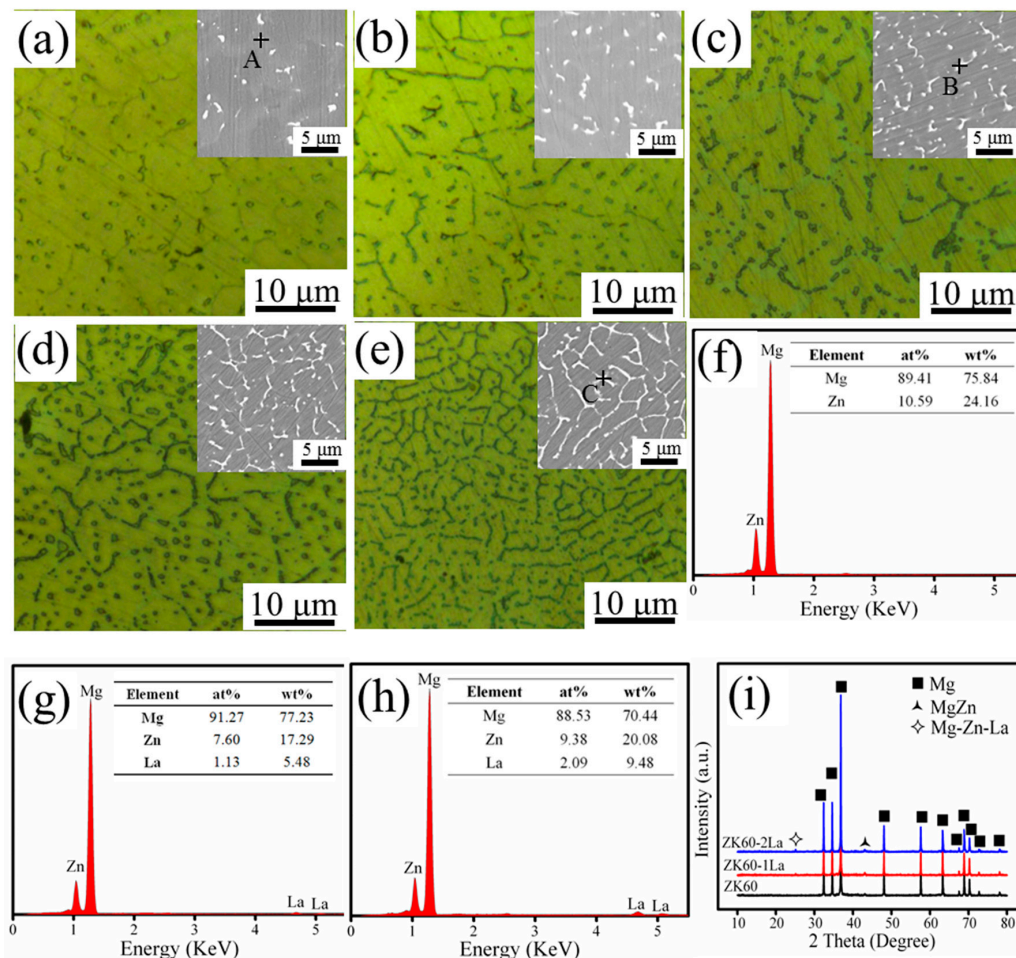


Figure 7. The metallurgical structure of (a) ZK60; (b) ZK60-0.5La; (c) ZK60-1.0La; (d) ZK60-1.5La; (e) ZK60-2.0La; EDS results of the secondary phase indicated by the points; (f) point A in Figure 7a; (g) point B in Figure 7c; (h) point C in Figure 7e; (i) XRD spectra of the samples.

The distribution of the intermetallic phase was analyzed by SEM and EDS. The ZK60 constituted of the α -Mg phase and intermetallic phase. The intermetallic phase in ZK60 was sparsely distributed along grain boundary with an island-like structure. Some intermetallic phase with short-bar shape appeared after alloying 0.5 wt % or 1.0 wt % La and increased with the La content increasing. The intermetallic phase with short-bar shape was widened and gradually connected to form a semi-continuous network as La content reached 1.5 wt % or 2.0 wt %. The EDS results revealed that the phase with the island-like shape (point A in Figure 7a) was constituted of Mg (89.41 at. %) and Zn (10.59 at. %) (Figure 6f), and the phase with short-bar shape (point B in Figure 7c) was constituted of Mg (91.27 at. %), Zn (7.60 at. %) and La (1.13 at. %) (Figure 7g). The phase with semi-continuous network shape (point C in Figure 7e) was constituted of Mg (88.53 at. %), Zn (9.38 at. %) and La (2.09 at. %) (Figure 7h). The XRD spectra of the samples were presented in Figure 7i. Combined with the EDS results, the phase with island-like shape was suggested to be MgZn, the phase with short-bar shape and phase with semi-continuous network shape was suggested to be the MgZnLa phase.

3.4. Mechanical Properties

The mechanical properties of the samples are shown in Figure 8. The compressive strength of ZK60, ZK60-0.5La, ZK60-1.0La, ZK60-1.5La, and ZK60-2.0La was 134.5 ± 4.5 MPa, 151.2 ± 4.3 MPa, 169.4 ± 5.1 MPa, 163.7 ± 4.5 MPa, and 158.8 ± 5.0 MPa, respectively. The compressive strength increased as the La content increased, and ZK60-1.0La possessed the highest compressive strength. The enhanced compression strength was partly ascribed to the strengthening effect of grain refinement and uniformly dispersed MgZnLa phase with short-bar shape. When the La content increased further, the compressive strength decreased. It was ascribed to the fact that continuity of the Mg matrix was destroyed by the semi-continuous network MgZnLa phase along the grain boundary, and stress accumulation could form at the interfaces between the MgZnLa phase and matrix during plastic deformation. In addition, with the increase of La content, the hardness of the samples increased from 83.9 ± 3.5 Hv for ZK60 to 104.9 ± 5.2 Hv for the ZK60-2.0La. It was attributed to the strengthening effect of grain refinement and precipitation strengthening of the high hardness MgZnLa phase.

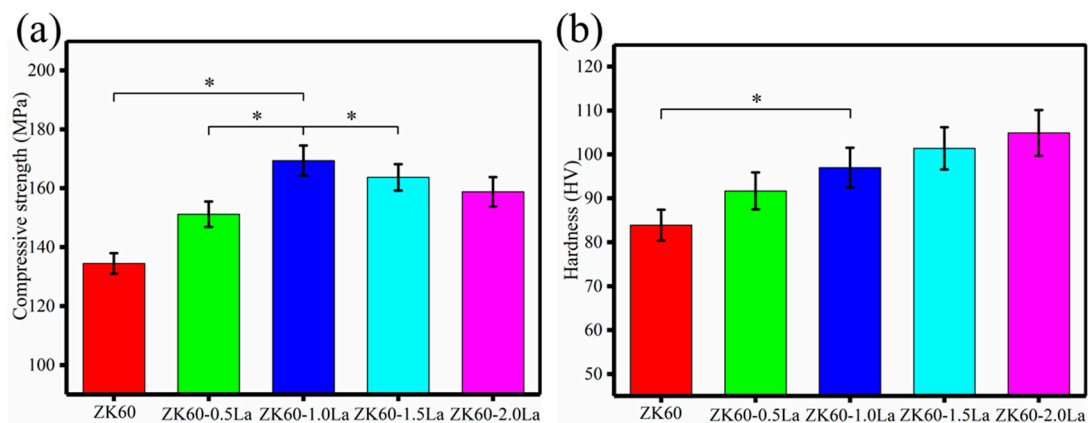


Figure 8. The mechanical properties of ZK60 and ZK60-La: (a) Compressive strength, (b) Hardness.

4. Conclusions

In this study, ZK60-La was successfully prepared by selective laser melting technology. ZK60-1.0La revealed a high cell inhibition rate of 61.9% for bone tumor cells and high cell viability of 91.9% for normal kidney cells, indicating its good anti-tumor properties. It further revealed that the MMP of U2OS cells after incubating in ZK60-La extracts was reduced as the La content increased. Meanwhile, the ROS levels in U2OS cells after incubating in the ZK60-La extracts increased with the La content increasing. In addition, its degradation rate 1.23 mm/year was lower than that of ZK60 alloy 2.13 mm/year, which was mainly attributed to the grain refinement.

Author Contributions: C.S. and L.Y. conceived and designed the experiments; L.L., C.G., and Y.Y. performed the experiments; S.P. analyzed the data; M.Z. and L.Y. contributed analysis tools; C.S. and L.L. wrote the paper. All authors reviewed the final manuscript.

Funding: This research was funded by the following funds: (1) The Natural Science Foundation of China [81871494, 51575537, 81572577, 81871498, 51705540]; (2) Hunan Provincial Natural Science Foundation of China [2016JJ1027, 2018JJ3671]; (3) Guangdong Province Higher Vocational Colleges & Schools Pearl River Scholar Funded Scheme [2018]; (4) The Open-End Fund for the Valuable and Precision Instruments of Central South University; (5) The Project of Hunan Provincial Science and Technology Plan [2017RS3008]; and (6) The Fundamental Research Funds for the Central Universities of Central South University [2018zzts143].

Conflicts of Interest: The authors declare no conflict of interest.

References

1. Dang, W.; Li, T.; Li, B.; Ma, H.; Zhai, D.; Wang, X.; Chang, J.; Xiao, Y.; Wang, J.; Wu, C. A bifunctional scaffold with CuFeSe₂ nanocrystals for tumor therapy and bone reconstruction. *Biomaterials* **2018**, *160*, 92–106. [[CrossRef](#)] [[PubMed](#)]
2. Ma, H.; Jiang, C.; Zhai, D.; Luo, Y.; Chen, Y.; Lv, F.; Yi, Z.; Deng, Y.; Wang, J.; Chang, J. A bifunctional biomaterial with photothermal effect for tumor therapy and bone regeneration. *Adv. Funct. Mater.* **2016**, *26*, 1197–1208. [[CrossRef](#)]
3. Zhang, Y.; Zhai, D.; Xu, M.; Yao, Q.; Chang, J.; Wu, C. 3d-printed bioceramic scaffolds with Fe₃O₄/graphene oxide nanocomposite interface for hyperthermia therapy of bone tumor cells. *J. Mater. Chem. B* **2016**, *4*, 2874–2886. [[CrossRef](#)]
4. Ding, D.; Xie, Y.; Li, K.; Huang, L.; Zheng, X. Black plasma-sprayed Ta₂O₅ coatings with photothermal effect for bone tumor therapy. *Ceram. Int.* **2018**, *44*, 12002–12006. [[CrossRef](#)]
5. Lu, Y.; Li, M.; Li, L.; Wei, S.; Hu, X.; Wang, X.; Shan, G.; Zhang, Y.; Xia, H.; Yin, Q. High-activity chitosan/nano hydroxyapatite/zoledronic acid scaffolds for simultaneous tumor inhibition, bone repair and infection eradication. *Mater. Sci. Eng. C* **2018**, *82*, 225–233. [[CrossRef](#)] [[PubMed](#)]
6. Ma, H.; Li, T.; Huan, Z.; Zhang, M.; Yang, Z.; Wang, J.; Chang, J.; Wu, C. 3D printing of high-strength bioscaffolds for the synergistic treatment of bone cancer. *NPG Asia Mater.* **2018**, *10*, 31–44. [[CrossRef](#)]
7. Li, M.; Wang, W.; Zhu, Y.; Lu, Y.; Wan, P.; Yang, K.; Zhang, Y.; Mao, C. Molecular and cellular mechanisms for zoledronic acid-loaded magnesium-strontium alloys to inhibit giant cell tumors of bone. *Acta Biomater.* **2018**, *77*, 365–379. [[CrossRef](#)] [[PubMed](#)]
8. Kawanishi, S.; Hiraku, Y.; Pinlaor, S.; Ma, N. Oxidative and nitrative DNA damage in animals and patients with inflammatory diseases in relation to inflammation-related carcinogenesis. *Biol. Chem.* **2006**, *387*, 365–372. [[CrossRef](#)] [[PubMed](#)]
9. Song, J.; Li, J.; Qiao, J.; Jain, S.; Evers, B.M.; Chung, D.H. PKD prevents H₂O₂-induced apoptosis via NF-κB and p38 MAPK in RIE-1 cells. *Biochem. Biophys. Res. Commun.* **2009**, *378*, 610–614. [[CrossRef](#)] [[PubMed](#)]
10. Chen, G.; Wang, F.; Trachootham, D.; Huang, P. Preferential killing of cancer cells with mitochondrial dysfunction by natural compounds. *Mitochondrion* **2010**, *10*, 614–625. [[CrossRef](#)] [[PubMed](#)]
11. Huang, P. ROS stress in cancer cells and therapeutic implications. *Drug Resist. Updat.* **2004**, *7*, 97–110.
12. Li, Z.Y.; Yang, Y.; Ming, M.; Liu, B. Mitochondrial ROS generation for regulation of autophagic pathways in cancer. *Biochem. Biophys. Res. Commun.* **2011**, *414*, 5–8. [[CrossRef](#)] [[PubMed](#)]
13. Wang, H.; Zhang, Y.; Du, Y. Ovarian and breast cancer spheres are similar in transcriptomic features and sensitive to fenretinide. *BioMed Res. Int.* **2013**, *2013*, 510905–510915. [[CrossRef](#)] [[PubMed](#)]
14. Shen, L.; Lan, Z.; Sun, X.; Shi, L.; Liu, Q.; Ni, J. Proteomic analysis of lanthanum citrate-induced apoptosis in human cervical carcinoma siha cells. *Biometals* **2010**, *23*, 1179–1189. [[CrossRef](#)] [[PubMed](#)]
15. Yu, L.; Xiong, J.; Guo, L.; Miao, L.; Liu, S.; Guo, F. The effects of lanthanum chloride on proliferation and apoptosis of cervical cancer cells: Involvement of let-7a and miR-34a microRNAs. *Biometals* **2015**, *28*, 879–890. [[CrossRef](#)] [[PubMed](#)]
16. Zhang, H.; Wang, C.; Zhu, L.; Liu, X.; Zhang, G.; Yu, W.; Meng, X.; Chow, Y.T. Growth and Characterization of Series Nd:Gd_xLa_{1-x}VO₄ (x = 0.80, 0.60, 0.45) Crystals. *J. Mater. Res.* **2002**, *17*, 556–562. [[CrossRef](#)]
17. Sze, A.; Erickson, D.; Ren, L.; Li, D. Zeta-potential measurement using the smoluchowski equation and the slope of the current-time relationship in electroosmotic flow. *J. Colloid Interface Sci.* **2003**, *261*, 402–410. [[CrossRef](#)]

18. Wang, L.; Ji, B.; Hu, Y.; Liu, R.; Sun, W. A review on in situ phytoremediation of mine tailings. *Chemosphere* **2017**, *184*, 594–600. [[CrossRef](#)] [[PubMed](#)]
19. Hu, J.; Jia, X.; Li, Q.; Yang, X.; Wang, K. Binding of La^{3+} to calmodulin and its effects on the interaction between calmodulin and calmodulin binding peptide, Polistes Mastoparan. *Biochemistry* **2004**, *43*, 2688–2698. [[CrossRef](#)] [[PubMed](#)]
20. Dong, S.; Zhao, Y.; Liu, H.; Yang, X.; Wang, K. Duality of effect of La^{3+} on mitochondrial permeability transition pore depending on the concentration. *Biometals* **2009**, *22*, 917–926. [[CrossRef](#)] [[PubMed](#)]
21. Heffeter, P.; Jakupec, M.A.; Körner, W.; Wild, S.; von Keyserlingk, N.G.; Elbling, L.; Zorbas, H.; Korynevskaya, A.; Knasmüller, S.; Sutterlüty, H. Anticancer activity of the lanthanum compound [tris (1, 10-phenanthroline) lanthanum (III)] trithiocyanate (KP772; FFC24). *Biochem. Pharmacol.* **2006**, *71*, 426–440. [[CrossRef](#)] [[PubMed](#)]
22. Chen, H.; Liu, S.; Miao, L.; Yu, L.; Wang, Y.; Guo, F. Inhibitory effect of lanthanum chloride on migration and invasion of cervical cancer cells. *J. Rare Earths* **2013**, *31*, 94–100. [[CrossRef](#)]
23. Gao, C.; Peng, S.; Feng, P.; Shuai, C. Bone biomaterials and interactions with stem cells. *Bone Res.* **2017**, *5*, 17059–17091. [[CrossRef](#)] [[PubMed](#)]
24. Liu, L.; Gebresellasie, K.; Collins, B.; Zhang, H.; Yun, Y. Degradation rates of pure zinc, magnesium, and magnesium alloys measured by volume loss, mass loss, and hydrogen evolution. *Appl. Sci.* **2018**, *8*, 1459. [[CrossRef](#)]
25. Parande, G.; Manakari, V.; Gupta, H.; Gupta, M. Magnesium- β -tricalcium phosphate composites as a potential orthopedic implant: A mechanical/damping/immersion perspective. *Metals* **2018**, *8*, 343. [[CrossRef](#)]
26. Xiong, H.; Liang, Z.; Wang, Z.; Qin, C.; Zhao, W.; Yu, H. Mechanical properties and degradation behavior of $\text{Mg}_{(100-7x)}\text{Zn}_{6x}\text{Y}_{x(x=0.2,0.4,0.6,0.8)}$ alloys. *Metals* **2018**, *8*, 261. [[CrossRef](#)]
27. Yang, Y.; Guo, X.; He, C.; Gao, C.; Shuai, C. Regulating degradation behavior by incorporating mesoporous silica for mg bone implants. *ACS Biomater. Sci. Eng.* **2018**, *4*, 1046–1054. [[CrossRef](#)]
28. Cao, N.Q.; Pham, D.N.; Kai, N.; Dinh, H.V.; Hiromoto, S.; Kobayashi, E. In vitro corrosion properties of Mg matrix in situ composites fabricated by spark plasma sintering. *Metals* **2017**, *7*, 358. [[CrossRef](#)]
29. Yang, Y.; Wu, P.; Wang, Q.; Wu, H.; Liu, Y.; Deng, Y.; Zhou, Y.; Shuai, C. The enhancement of Mg corrosion resistance by alloying Mn and laser-melting. *Materials* **2016**, *9*, 216. [[CrossRef](#)] [[PubMed](#)]
30. Sun, W.; Zhang, G.; Tan, L.; Yang, K.; Ai, H. The fluoride coated AZ31B magnesium alloy improves corrosion resistance and stimulates bone formation in rabbit model. *Mat. Sci. Eng. C* **2016**, *63*, 506–511. [[CrossRef](#)] [[PubMed](#)]
31. Pu, S.; Chen, M.; Chen, Y.; Zhang, W.; Soliman, H.; Qu, A.; Liu, Q.; Tang, X.; Huang, N.; Wan, G. Zirconium ions integrated in 1-hydroxyethylidene-1,1-diphosphonic acid (HEDP) as a metalorganic-like complex coating on biodegradable magnesium for corrosion control. *Corros. Sci.* **2018**, *144*, 277–287. [[CrossRef](#)]
32. Weizbauer, A.; Seitz, J.-M.; Werle, P.; Hegermann, J.; Willbold, E.; Eifler, R.; Windhagen, H.; Reifenrath, J.; Waizy, H. Novel magnesium alloy Mg-2La caused no cytotoxic effects on cells in physiological conditions. *Mater. Sci. Eng. C* **2014**, *41*, 267–273. [[CrossRef](#)] [[PubMed](#)]
33. Myrissa, A.; Agha, N.A.; Lu, Y.; Martinelli, E.; Eichler, J.; Szakacs, G.; Kleinhans, C.; Willumeit-Römer, R.; Schäfer, U.; Weinberg, A.-M. In vitro and in vivo comparison of binary Mg alloys and pure Mg. *Mater. Sci. Eng. C* **2016**, *61*, 865–874. [[CrossRef](#)] [[PubMed](#)]
34. Zhang, Y.; Li, J.Y.; Liaw, P.K.; Xu, Y.Z.; Lai, H.Y. Effects of heat treatment on the mechanical properties and corrosion behaviour of the $\text{Mg-2Zn}_{n-0.2}\text{Mn}_{-x}\text{Nd}$ alloys. *J. Alloys Compd.* **2018**, *769*, 552–565. [[CrossRef](#)]
35. Zhang, Y.; Li, J.; Lai, H.; Xu, Y. Effect of homogenization on microstructure characteristics, corrosion and biocompatibility of Mg-Zn-Mn-xCa alloys. *Materials* **2018**, *11*, 227. [[CrossRef](#)] [[PubMed](#)]
36. Yang, Y.; Wu, P.; Lin, X.; Liu, Y.; Bian, H.; Zhou, Y.; Gao, C.; Shuai, C. System development, formability quality and microstructure evolution of selective laser-melted magnesium. *Virtual Phys. Prototyp.* **2016**, *11*, 173–181. [[CrossRef](#)]
37. Jiang, B.; Xiang, Q.; Atrons, A.; Song, J.; Pan, F. Influence of crystallographic texture and grain size on the corrosion behaviour of as-extruded mg alloy AZ31 sheets. *Corros. Sci.* **2017**, *126*, 374–380. [[CrossRef](#)]
38. Ding, Y.; Lin, J.; Wen, C.; Zhang, D.; Li, Y. Mechanical properties, in vitro corrosion and biocompatibility of newly developed biodegradable Mg-Zr-Sr-Ho alloys for biomedical applications. *Sci. Rep.* **2016**, *6*, 31990–31999. [[CrossRef](#)] [[PubMed](#)]

39. *Biological Evaluation of Medical Devices-Part 5: Tests for In Vitro Cytotoxicity*; British Standard BS EN ISO 10993-5. 1999; British Standards Institute: London, UK, 2009.
40. Willbold, E.; Gu, X.; Albert, D.; Kalla, K.; Bobe, K.; Brauneis, M.; Janning, C.; Nellesen, J.; Czayka, W.; Tillmann, W. Effect of the addition of low rare earth elements (lanthanum, neodymium, cerium) on the biodegradation and biocompatibility of magnesium. *Acta Biomater.* **2015**, *11*, 554–562. [[CrossRef](#)] [[PubMed](#)]
41. Fitzpatrick, L.A. Differences in the actions of calcium versus lanthanum to influence parathyroid hormone release. *Endocrinology* **1990**, *127*, 711–715. [[CrossRef](#)] [[PubMed](#)]
42. Weiss, G.B. Cellular pharmacology of lanthanum. *Annu. Rev. Pharmacol.* **1974**, *14*, 343–354. [[CrossRef](#)]
43. Liu, H.; Yuan, L.; Yang, X.; Wang, K. La^{3+} , Gd^{3+} and Yb^{3+} induced changes in mitochondrial structure, membrane permeability, cytochrome c release and intracellular ROS level. *Chemico-Biol. Interact.* **2003**, *146*, 27–37. [[CrossRef](#)]
44. Orzolek, A.; Wysocki, P.; Strzeżek, J.; Kordan, W. Superoxide dismutase (SOD) in boar spermatozoa: Purification, biochemical properties and changes in activity during semen storage (16 °C) in different extenders. *Reprod. Biol.* **2013**, *13*, 34–40. [[CrossRef](#)] [[PubMed](#)]
45. Perillo, B.; Di Santi, A.; Cerner, G.; Ombra, M.N.; Castoria, G.; Migliaccio, A. Nuclear receptor-induced transcription is driven by spatially and timely restricted waves of ROS: The role of Akt, IKK α , and DNA damage repair enzymes. *Nucleus* **2014**, *5*, 482–491. [[CrossRef](#)] [[PubMed](#)]
46. Clement, J.A. *Studies of Bioactive Natural Products and Mechanism-Based Bioassays*. Ph.D. Thesis, Virginia Tech, Blacksburg, VA, USA, 2005.



© 2018 by the authors. Licensee MDPI, Basel, Switzerland. This article is an open access article distributed under the terms and conditions of the Creative Commons Attribution (CC BY) license (<http://creativecommons.org/licenses/by/4.0/>).